

Supplementary Information

Visualization and evaluation of lithium diffusion at the grain boundaries in $\text{Li}_{0.29}\text{La}_{0.57}\text{TiO}_3$ solid electrolytes using secondary ion mass spectrometry

Gen Hasegawa, Naoaki Kuwata, Tsuyoshi Ohnishi, Kazunori Takada

Center for Green Research on Energy and Environmental Materials, National Institute for Materials

Science (NIMS), 1-1 Namiki, Tsukuba, Ibaraki 305-0044, JAPAN

Scanning electron microscopy-electron backscatter diffraction (SEM-EBSD)

$\text{Li}_{0.29}\text{La}_{0.57}\text{TiO}_3$ (LLTO) was observed using SEM, and the grains were visualized using EBSD.

SEM and EBSD were conducted using a JSM-7800F spectrometer (JEOL, Tokyo, Japan) with an AZtec EBSD system (Oxford Instruments, Abingdon, UK).

In the sample, rutile TiO_2 is observed, in addition to LLTO (Fig. S1b), and the average diameter of the LLTO particles is $16\ \mu\text{m}$ (Fig. S1d). Furthermore, EBSD reveals that approximately 10% of the coincidence site lattice (CSL) boundaries exhibit Σ values of $\leq \Sigma 29$ (Fig. S1e, f).

As shown in Fig. S1b, polycrystalline LLTO contains TiO_2 as a second phase, which is observed as a light gray area in the optical microscope image shown in Fig. 3c. The SIMS measurements did not reveal any significant changes around TiO_2 . Therefore, this phase is regarded as a volume in which Li^+ ions cannot diffuse as effectively as voids.

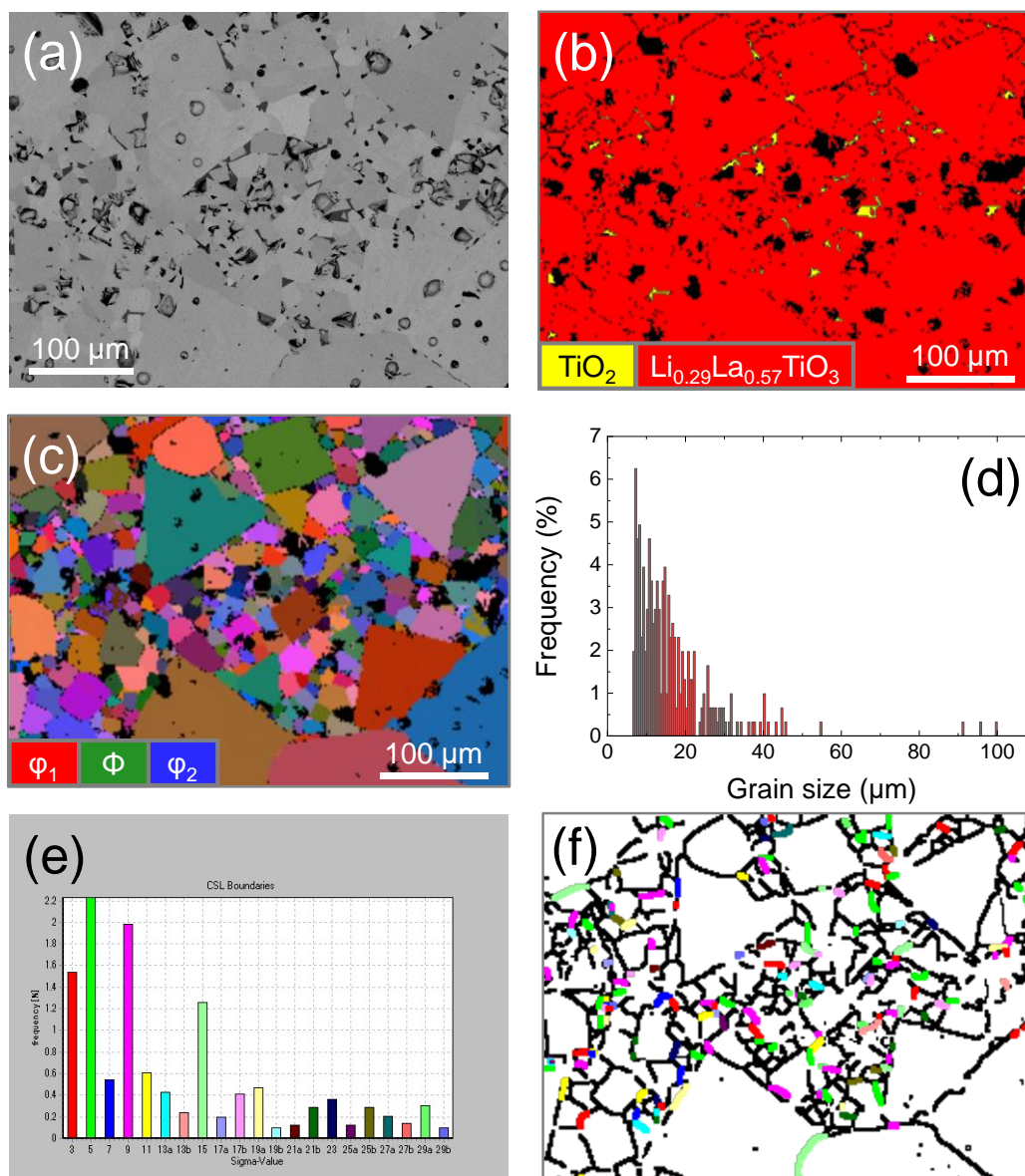


Figure S1. (a) SEM image of the surface of LLTO. (b) Color map of the crystalline phases obtained via EBSD. The red and yellow regions indicate perovskite-type LLTO and rutile-type TiO_2 , respectively. (c) Euler color map obtained using EBSD. (d) Frequency of the grain size in LLTO using EBSD. (e) Frequencies of the CSL boundaries, based on EBSD. (f) Spatial distribution of the CSL boundaries. The relationship between Σ and color is the same as that shown in Fig. S1e. The black lines represent random grain boundaries with Σ values of $>\Sigma_{29}$.

Measurement of the bulk and grain boundary conductivities using impedance spectroscopy

The ionic conductivity was measured via impedance spectroscopy using a high-frequency impedance system (4990EDMS-120K, TOYO, Tokyo, Japan) in the respective frequency and temperature ranges 10–10⁸ Hz and 200–470 K. A high-temperature system (ProboStat, NORECS, Oslo, Norway) equipped with an impedance analyzer (1260A, Solartron Analytical, Farnborough, UK) was used for measurements between 470 and 734 K in the frequency range 0–10 Hz. Thin Au electrodes were sputtered onto both sides of the polished samples.

Fig. S2a shows the Nyquist plot of the resistance at 300 K. The impedance components are attributed to the bulk (>50 kHz), grain boundary (0.5–50 kHz), and electrode interface (<0.5 kHz). The bulk (σ_{bulk}) and grain boundary (σ_{gb}) conductivities were determined using the equivalent circuit shown in Fig. S2b. Table S1 shows the temperature dependences of σ_{bulk} , σ_{gb} , and the conductivity diffusion coefficients calculated using the Nernst-Einstein equation.

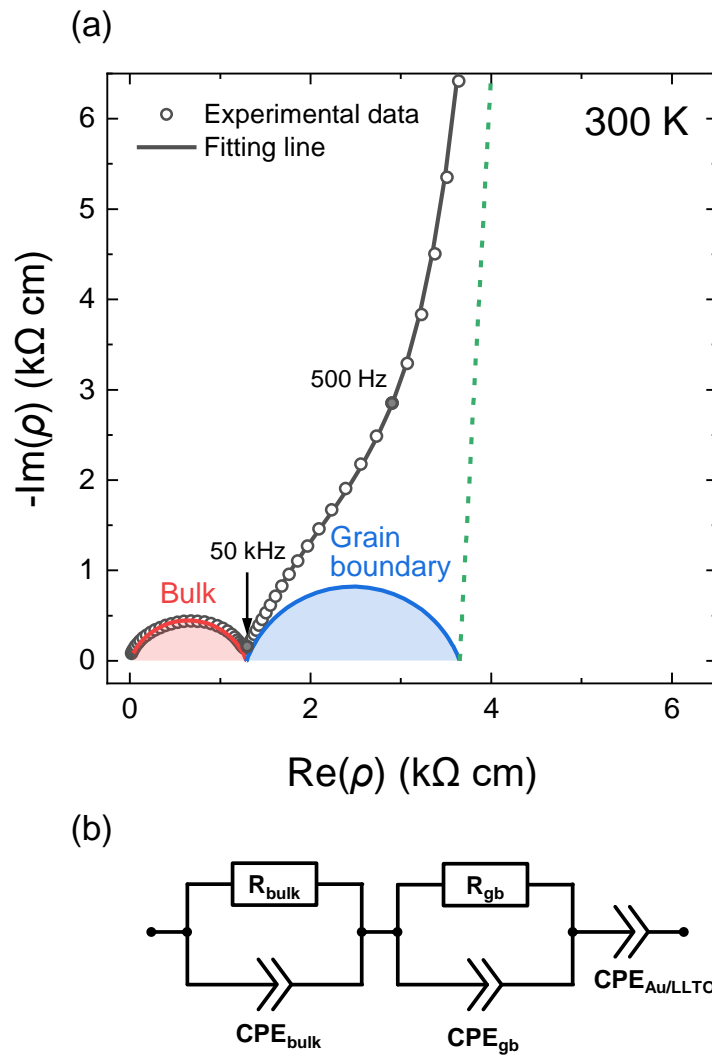


Figure S2. (a) Nyquist plot of the LLTO polycrystals at 300 K. (b) Equivalent circuit of an LLTO polycrystal.

Table S1. Temperature dependences of the bulk and grain boundary conductivities.

Temperature (K)	σ_{bulk} (S cm ⁻¹)	σ_{gb} (S cm ⁻¹)	$D_{\sigma,\text{bulk}}$ (cm ² s ⁻¹)	$D_{\sigma,\text{gb}}$ (cm ² s ⁻¹)
219.8	8.26×10^{-6}	1.41×10^{-6}	1.96×10^{-10}	3.34×10^{-11}
239.8	3.61×10^{-5}	8.70×10^{-6}	9.34×10^{-10}	2.25×10^{-10}
240.2	3.70×10^{-5}	3.75×10^{-5}	9.57×10^{-10}	1.05×10^{-9}
260.1	1.25×10^{-4}	1.35×10^{-4}	3.49×10^{-9}	4.08×10^{-9}
280.3	3.62×10^{-4}	4.20×10^{-4}	1.09×10^{-8}	1.36×10^{-8}
300.2	8.80×10^{-4}	4.12×10^{-4}	2.85×10^{-8}	1.33×10^{-8}
320.3	1.94×10^{-3}	1.11×10^{-3}	6.71×10^{-8}	3.80×10^{-8}
340.3	3.80×10^{-3}	3.02×10^{-3}	1.40×10^{-7}	1.11×10^{-7}
360.3	6.76×10^{-3}	5.69×10^{-3}	2.63×10^{-7}	2.21×10^{-7}
380.4	1.12×10^{-2}	1.10×10^{-2}	4.59×10^{-7}	4.49×10^{-7}
400.5	1.71×10^{-2}	1.75×10^{-2}	7.40×10^{-7}	7.55×10^{-7}
420.3	2.40×10^{-2}	3.16×10^{-2}	1.09×10^{-6}	1.43×10^{-6}
440.4	3.24×10^{-2}	5.81×10^{-2}	1.54×10^{-6}	2.76×10^{-6}
460.4	4.29×10^{-2}	7.78×10^{-2}	2.13×10^{-6}	3.86×10^{-6}
470.7	4.78×10^{-2}	1.07×10^{-1}	2.43×10^{-6}	5.44×10^{-6}
489.2	4.70×10^{-2}	-	2.48×10^{-6}	-
589.7	8.88×10^{-2}	-	5.64×10^{-6}	-
689.5	1.23×10^{-1}	-	9.17×10^{-6}	-
734.4	1.38×10^{-1}	-	1.10×10^{-5}	-

Grain boundary diffusion coefficients determined from SIMS imaging

Similar line analyses were performed at other grain boundaries. The results are shown in Fig. S3 and

Table S2. The D_{gb}^* values for each grain boundary are in the range of 2.6×10^{-14} to $1.5 \times 10^{-13} \text{ cm}^2 \text{ s}^{-1}$

and are within the error bars shown in Fig. 5 (b) and (c). The average value is $6.8 \times 10^{-14} \text{ cm}^2 \text{ s}^{-1}$.

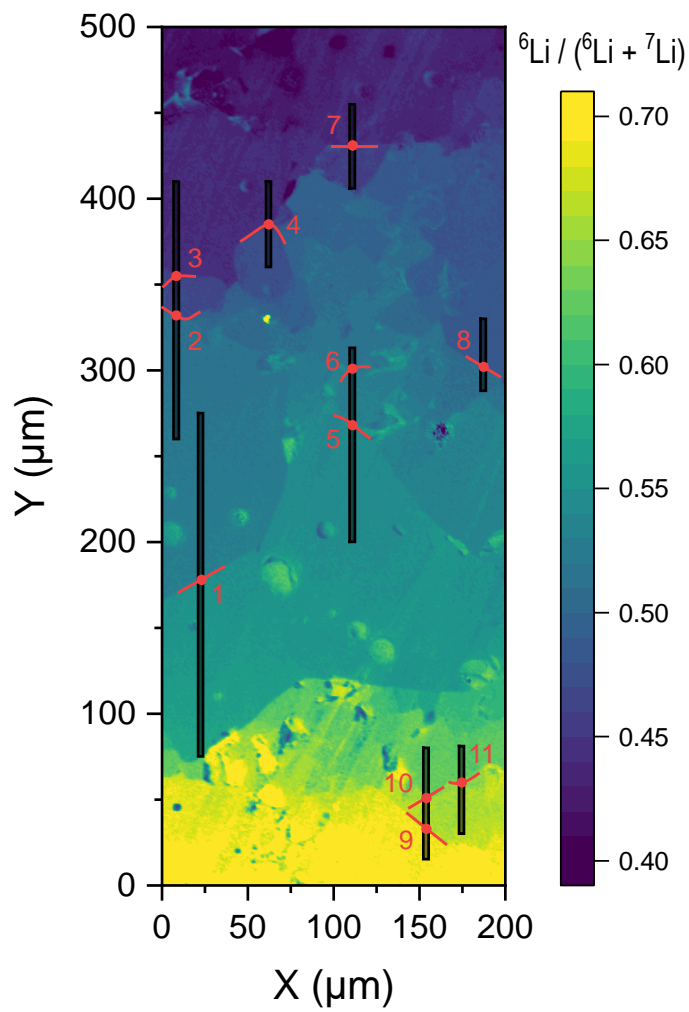


Figure S3. Position where the grain boundary diffusion coefficient is determined.

Table S2. Grain boundary diffusion coefficients in SIMS imaging (Fig. S3)

Number	X (μm)	Y (μm)	D_{gb}^*/δ (cm s^{-1})	$(l/\delta)D_{\text{gb}}^*$ ($\text{cm}^2 \text{s}^{-1}$)	D_{gb}^* ($\text{cm}^2 \text{s}^{-1}$)
1	15	172	1.5×10^{-6}	2.5×10^{-9}	7.6×10^{-14}
2	8	332	1.2×10^{-6}	2.0×10^{-9}	6.1×10^{-14}
3	8	355	2.9×10^{-6}	4.9×10^{-9}	1.5×10^{-13}
4	62	385	8.2×10^{-7}	1.4×10^{-9}	4.1×10^{-14}
5	111	268	1.1×10^{-6}	1.9×10^{-9}	5.7×10^{-14}
6	111	431	6.0×10^{-7}	9.9×10^{-10}	3.0×10^{-14}
7	111	301	5.2×10^{-7}	8.7×10^{-10}	2.6×10^{-14}
8	187	302	9.4×10^{-7}	1.6×10^{-9}	4.7×10^{-14}
9	154	33	1.4×10^{-6}	2.4×10^{-9}	7.2×10^{-14}
10	154	51	2.7×10^{-6}	4.4×10^{-9}	1.3×10^{-13}
11	175	60	1.2×10^{-6}	1.9×10^{-9}	5.8×10^{-14}